

SUBMISSION TO
ENGINEERING GEOLOGY JOURNAL

DATE: Written 1 November 2018

TITLE:

Desiccation behaviour of colloidal silica grouted sand: A new material for the creation of near surface hydraulic barriers.

AUTHORS:

Matteo Pedrotti*

Christopher Wong**

Gráinne El Mountassir***

Joanna C. Renshaw*

Rebecca J. Lunn****

POSITION AND AFFILIATION:

* Chancellor's Fellow, Department of Civil and Environmental Engineering, University of Strathclyde

** PhD Candidate, Department of Civil and Environmental Engineering, University of Strathclyde

*** Senior Lecturer, Department of Civil and Environmental Engineering, University of Strathclyde

**** Professor, Department of Civil and Environmental Engineering, University of Strathclyde

CONTACT ADDRESS:

Dr. Matteo Pedrotti

Department of Civil and Environmental Engineering

University of Strathclyde

James Weir Building - Level 5

75 Montrose Street - Glasgow G1 1XJ, Scotland, UK

E-mail: matteo.pedrotti@strath.ac.uk

KEYWORDS

Hydraulic barrier, colloidal silica grouting; drying; x-ray tomography; hydraulic conductivity; water retention curve

ABSTRACT

This paper considers the mechanism of cracking in colloidal silica (CS) grout subjected to drying and wetting cycles, with the aim of testing its use for the creation of near-surface low hydraulic conductivity barriers for applications in nuclear decommissioning. The advantage in this context of CS over more traditional materials, such as clay liners or geotextiles, are its capability to permeate into in situ soils at low injection pressures and injectability within and beneath regions of existing contamination, thus reducing cost and removing any requirement for excavation and disposal of hazardous materials.

In near-surface applications, hydraulic barriers are exposed to natural climatic variations, in the form of cycles of drying and wetting, which can result in cracking of the barrier material and a subsequent increase in the hydraulic conductivity. Ultimately, this reduces their ability to perform their end function. The aims of this paper are to study the mechanism of crack formation in colloidal silica grout barriers when exposed to severe drying and wetting cycles and to determine the effect on its hydraulic properties. To achieve these aims, grouted soil samples were created and exposed to severe drying and re-wetting. Samples were tested for hydraulic conductivity at each stage and 3D images of the pore structure were obtained from micro X-ray CT scanning. On drying, nanoscale cracks form within the CS matrix, which are 10s of nanometres in width, these have an associated air- entry value of ~20,000kPa. Additional meso-scale cracks can also form in CS filled pores when surrounded by sand grains, due to conditions of restrained shrinkage. These cracks are typically hundreds of microns in width and

have an associated air-entry value of ~200kPa. X-ray CT analysis of the connectivity of this meso-scale pore space, filled by air after drying, indicates that although cracks form, a connected network does not, thus explaining the observation that even after severe drying the CS grouted sand retains a very low hydraulic conductivity.

1. INTRODUCTION

This paper proposes the use of colloidal silica (CS) grout to create injectable low hydraulic conductivity barriers in soil, with a particular focus on creating barriers for applications in nuclear decommissioning. Worldwide, nuclear decommissioning is of major concern. According to the International Energy Agency, by 2040 almost 200 reactors are planned for shut-down (Green, 2017). In the UK, the Nuclear Decommissioning Authority estimate the cost of nuclear decommissioning to be £121 billion, with activities ongoing for a period of 120 years (Mulholland et al., 2019). As a consequence, any technology that can limit the migration of radioactive contaminants in the ground over this time period has the potential to bring significant cost savings.

In modern infrastructure, sophisticated containment technologies are used to prevent water and soil contamination in areas where contaminants might enter into contact with groundwater and soil. However, on nuclear legacy sites, containment can be poor. On some sites radioactive contaminants are in direct contact with the surrounding soil (e.g. in unlined trenches), thus posing a high risk of soil and groundwater contamination. Additionally, silos, ponds, underground pipes and storage tanks are all forms of infrastructure where contaminants are generally separated from the surrounding soil by cement barriers (e.g. cement walls). Over a facility's life span, cement barriers have been exposed to elevated radiation, thermal shock, chemical attack and ageing, with the result that over time the barrier may have become compromised, leading to an increased risk of groundwater contamination.

To limit the migration of contaminants for radioactively contaminated sites it is desirable to enhance or remediate existing containment structures. Subsurface hydraulic barriers are conventionally created by deploying compacted clays, geosynthetic clay liners or bentonite

enhanced sand mixtures. However, these technologies require ground excavation, which limits their use on sites with existing contamination, since barrier installation is not feasible without excavation of the contaminated volume. Excavation presents both an economic limitation and a technical challenge, as hazardous and contaminated material must be safely handled and disposed of, worker exposure needs must be minimised and sites are often congested and not easily accessible (e.g. the Sellafield site, UK).

Grout injection technologies present a valid alternative to clay barriers since they minimize the risks associated with contaminant handling. Jet grouting and permeation grouting are two general techniques for creating grout barriers. Jet grouting involves the injection of grout (+/- air/ air and water) at high injection pressures and at high velocity which cuts up the existing soil and mixes with it to form cemented bodies (or columns). During jet grouting excess eroded soil is lifted to the surface and as such handling and disposal of contaminated material still needs to be considered. Furthermore, the process is highly disruptive to the ground and can result in ground heave (e.g. Chai et al., 2005), which is not suitable in proximity to existing ageing containment infrastructure on nuclear sites, as they may become damaged, creating additional leakage pathways. Permeation grouting is the injection of a low viscosity grout to fill the free porosity within the ground (Truex et al., 2011). Cementitious grouts are not suitable for permeation near-surface (at depths less than ~10m) as their rheology (often modelled as a Bingham fluid), initial high viscosity, and coarse particle size, requires high injection pressures to initiate flow, which can induce ground heave. Chemical grouts, by contrast, are easier to inject than cement grouts as they are not particulate suspensions and have lower initial viscosities. However, chemical grouts are often expensive, exhibit syneresis and may contain toxic components (Gallagher et al., 2013). Colloidal silica represents an exception to other grouts, since it has a low initial viscosity (close to that of water) a very small particle size

(<100nm) and is chemically simple and non-toxic.

Gallagher et al. (2013) conducted a life cycle assessment comparing the installation of a colloidal silica injected barrier and a jet grouted cement barrier at a US superfund site with low level radionuclide contamination. They give detailed estimates of costs for both systems, although the material cost for colloidal silica is higher than that of cement (2.7 times higher), it is off-set by lower costs associated with permeation grouting equipment compared to jet grouting equipment and no costs associated with disposal of contaminated soil when installing a colloidal silica injected barrier. Furthermore the colloidal silica injected barrier was shown to have an overall better environmental performance than that of the jet-grouted cement barrier.

2. COLLOIDAL SILICA

As highlighted in Wong et al. (2018), colloidal silica's low initial viscosity, the possibility of tailoring the gel time (Pedrotti et al., 2017) and a particle size of the order of tens of nanometers (Iler, 1979) all make CS an attractive grouting material, especially for near surface applications where low injection pressures are required. Additionally, the low hydraulic conductivity of the gelled silica (below 10^{-10} m/s) and that fact that it is environmentally inert (Moridis et al., 1995), make CS very suitable as an impermeable barrier material that could be injected beneath existing waste storage facilities, such as unlined trenches.

CS grout was first used within the petroleum industry (Jurinak and Summers, 1991) for controlling fluid flow around wellbores. Subsequently, during the second half of the 90s, the Lawrence Berkeley National Laboratory research group investigated its use as a permeation grout for contaminated sites (Persoff et al., 1995, Moridis et al., 1995, Moridis et al., 1996, Hakem et al., 1997, Moridis et al., 1999, Persoff et al., 1999, Manchester et al., 2001). Eventually, CS had its breakthrough in tunnelling and underground construction, where it has

been commercially deployed as pre-injection material (e.g. Bahadur et al. (2007) and Butrón et al. (2010)) to prevent water ingress and for soil stabilization.

Wong et al. (2018) reviewed previous research on the mechanical behaviour of colloidal silica grouted soil (Gallagher and Mitchell (2002), Liao et al. (2003), Axelsson (2006), Gallagher et al. (2007), Butrón et al. (2009), Mollamahmutoglu and Yilmaz (2010), Changizi and Haddad (2017)) and presented direct shear and oedometer results to characterise the mechanical performance of CS-grouted sand and mixed CS-clay systems. We showed that in saturated conditions, CS is suitable for use in stabilising temporary works. In order to guarantee long-term performance of such temporary works, it is crucial to understand the wetting and drying behaviour of CS-grouted soils.

Near-surface hydraulic barrier integrity can be compromised over long timescales by desiccation cracking, as a consequence of drying and wetting cycles (Hewitt and Philip, 1999, Tang et al., 2010, Costa et al., 2013, Safari et al., 2014, Li et al., 2016). Many studies have shown an abrupt increase the hydraulic conductivity of clay barriers once cracking has occurred, sometimes up to 500 times the original permeability (Boynton and Daniel, 1985, Kleppe and Olson, 1985, Omidy et al., 1996, Hewitt and Philip, 1999, Albrecht and Benson, 2001, Albright et al., 2006, Rayhani et al., 2007, Meer and Benson, 2007, Henken-Mellies and Schweizer, 2011, He et al., 2015).

To-date, no research has been published on the water retention properties of colloidal silica-soil systems, nor on their temporal hydraulic conductivity evolution upon drying and wetting cycles. This paper investigates the evolution of the pore structure and the hydraulic conductivity of CS grouted sand subjected to a severe drying and wetting cycle. The aim is to understand the benefits and the drawbacks associated with the use of colloidal silica grout in near-surface barrier applications, where drying and wetting patterns may pose a severe risk to

barrier integrity. In order to illuminate CS behaviour, the paper presents a microstructural study on the mechanism of cracking of colloidal silica when coupled with a rigid hosting lattice, such as the one provided by sand. A sand lattice with oven-drying conditions was chosen, instead of a more general well-graded soil within a realistic climate, since this constitutes a worst case scenario, and is more extreme than would be encountered in the field; the oven-drying conditions will force the colloidal silica to crack within the open rigid lattice, allowing for investigation of the micromechanisms controlling the crack formation and propagation.

3. MATERIALS

The colloidal silica grout used in this research work, Meyco MP320 purchased from BASF, is described in Wong et al. (2018). Its basic characteristics are: 40% silica mass concentration, 15nm average particle size and 1.3 kg/l density. In the following experiments the accelerator concentration was designed according to the analytical model described in Pedrotti et al. (2017). A solution of 1.7 M of NaCl was added as an accelerator to gel the grout. The colloidal silica and the accelerator were hand mixed with a volume ratio of 5:1 (CS:accelerator) resulting in a gel time of approximately 1 hour.

The sand used in this research work is a medium coarse Leighton Buzzard sand with a d₅₀ of 1.2 mm, a specific gravity of 2.65 and a coefficient of uniformity of 1.26 was used for all tests. In every test the sand specimens were prepared by dry pluvial deposition from a height of not more than 10 cm. It is therefore considered that the relative density of the specimen was close to zero, as the sand was in its loosest state. Measurements of the porosity of the dry sand prior to grouting were consistently ~ 37%.

4. SAMPLE PREPARATIONS

This work presents the results of different experimental tests: i) water retention curves, ii) scanning electron microscope images, iii) X-ray tomography and iv) hydraulic conductivity tests.

Water retention curve and Scanning Electron Microscope Imaging

Water retention curves and Scanning Electron Microscope (SEM) images were performed on the same set of specimens. The specimens were prepared in plastic cups (Figure 1a) 37.5 mm in diameter and 8.5 mm tall. 6 specimens were prepared by filling the cups with CS grout only and 2 specimens were prepared with sand grouted with CS.

For the grouted specimens, each cup was filled with 14.13 g of Leighton Buzzard sand (Figure 1b). Subsequently, a 10-ml syringe was used to saturate the sand with 4.24 g of CS grout (Figure 1c). Immediately after this the cups were covered with parafilm® to prevent water evaporation during the gelling process.



Figure 1. Grouted sand specimen preparation for water retention curve. a) plastic cup, b) sand only and c) sand grouted with CS.

For SEM images, one of the specimens of CS only and one of the specimens of sand grouted with CS were used.

X-ray tomography and hydraulic conductivity test

A specimen of grouted sand was prepared in a hollow acrylic cylinder of 10 cm in diameter and 20 cm high. This sample was used for both X-ray tomography and hydraulic conductivity tests.

The cylinder was filled with Leighton Buzzard sand up to a height of 15 cm and then saturated with CS grout. During the grouting process CS was poured from the top of the sample and was allowed to permeate through the sample and flow out the bottom of the cylinder. As CS permeated, a constant hydraulic head of approximately 5 cm above the sand level was maintained for the duration of the injection. When the grout viscosity increased and the permeation stopped, the sample was covered with parafilm® to prevent evaporation and was left to cure for 1 week.

After curing, the thin layer of CS that had formed at the top of the specimen, was gently removed so as to leave only the grouted sand.

Additional hydraulic conductivity testing

A second set of grouted samples was prepared to test the hydraulic conductivity in a core holder with an applied confining pressure. A specimen of grouted sand was prepared in a hollow acrylic cylinder of 3 cm in diameter and 6 cm high. As with the previous sample, the mould was filled with Leighton Buzzard sand and then saturated with CS grout. The grouting procedure was as described above.

5. EXPERIMENTAL PROCEDURES

Water retention curve and Scanning Electron Microscope Imaging

A flow chart representing the different stages followed to obtain the water retention curve and SEM images is shown in Figure 3.

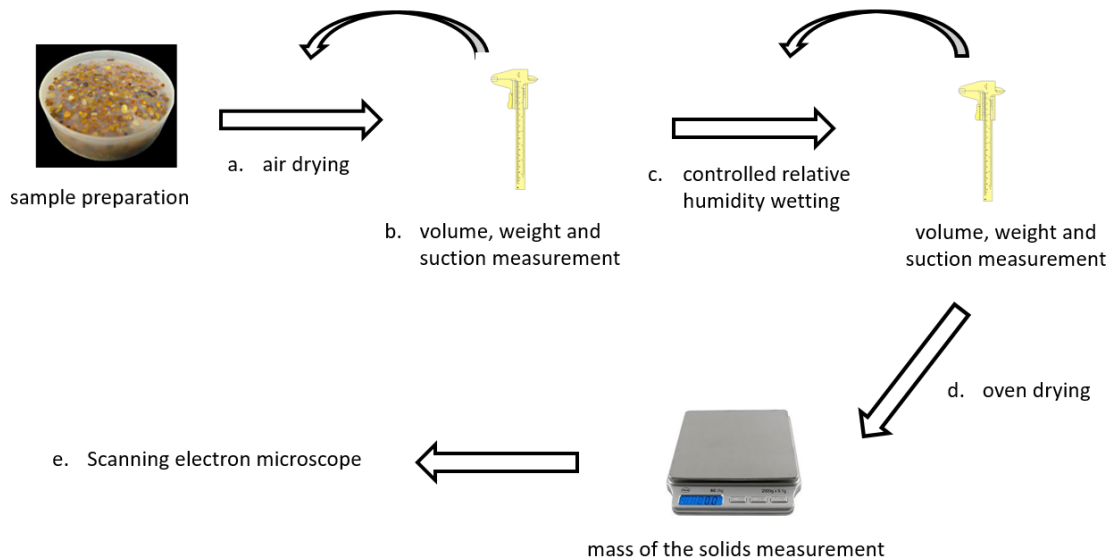


Figure 2. Experimental flow chart of procedure followed to obtain the water retention curve.

a. Air-drying. Specimens were progressively air dried under laboratory conditions at 20°C.

b. Volume, weight and suction measurements. After each drying step, the volume of the specimen was measured using Vernier callipers and the mass weighed using a bench-top balance. Total suction was measured using a WP4-C dew-point potentiometer (Decagon Device Inc). The WP4-C device measures total suction using the chilled-mirror dew-point technique. Accuracy of the dew point temperature measurements in the WP4-C for both the mirror and specimens are 0.001°C. This allows the WP4-C to provide total suction readings in the range of 10² kPa to 3·10⁵ kPa (Cobos and Chambers, 2010). The device has an internal

sealed chamber in to which specimens of size up to 12 cm³ are placed. Calibration standard salt solutions of potassium chloride and sodium chloride were used to calibrate the device according to the manufacturer's guidelines.

c. Controlled relative humidity wetting. After the drying path, the samples were wetted by storing in controlled environmental conditions of 90% relative humidity at 20 °C, for a minimum of 72 hours. A CS only specimen at the end of a drying-wetting cycle is shown in Figure 3a. Following completion of the wetting process, the procedure as described above was followed to measure suction with associated measurement of the specimen mass and volume. Following tests on CS only specimens, the relative humidity method was also used to preparing specimens along the wetting path for grouted sand.



Figure 3. Relative humidity hydration method. a) specimen after a drying and wetting cycle b) specimen after a drying-wetting-drying cycle.

d. Oven drying. At the end of the wetting path, the specimens were oven dried at 105°C for 24 hours for full dehydration (Figure 3b) and the final water content and mass of dry solids were determined.

For each water content, this procedure allowed the total volume, the volume of the solids, the volume of the voids and the volume occupied by the water to be calculated. The degree of saturation and void ratio could therefore be determined.

3 of the 6 CS specimens were oven-dried immediately after the drying path (stage b in Figure 2) and therefore only the drying behaviour was investigated. For the other 3 CS

specimens, the whole procedure described above (a drying-wetting-drying path) was followed.

e. Scanning Electron Microscope Imaging. One sample of CS and one sample of sand grouted with CS were analysed using a SEM. Microscope images were obtained by means of a Field Emission Scanning Electron Microscope (Hitachi SU-6600). This apparatus is equipped with energy dispersive spectroscopy, Oxford Inca 350 with 20mm X-Max detector and Wavelength dispersive spectroscopy, Oxford Inca Wave 700 microanalysis system with Energy to allow elemental analysis of metals and ceramic materials.

Microscope images were also obtained using a Tungsten Filament Scanning Electron Microscope (Hitachi S-3700). This apparatus has Energy Dispersive Spectroscopy capability, Oxford Inca 350 with 80mm X-Max detector, to allow elemental analyses of materials.

X-ray tomography and hydraulic conductivity test

As reported in Figure 4, X-ray tomography and hydraulic conductivity tests were performed on a column of grouted sand at different stages during a drying-wetting cycle. The hydraulic conductivity of the specimen was first measured under “as grouted” conditions (after a 1 week curing period). Following the initial hydraulic conductivity test, the specimen was X-ray scanned. Afterwards, the specimen was oven-dried and X-ray scanned again. Finally, the sample was saturated with water, the hydraulic conductivity was measured again and a final X-ray scan was performed.

The different stages are described in detail below.

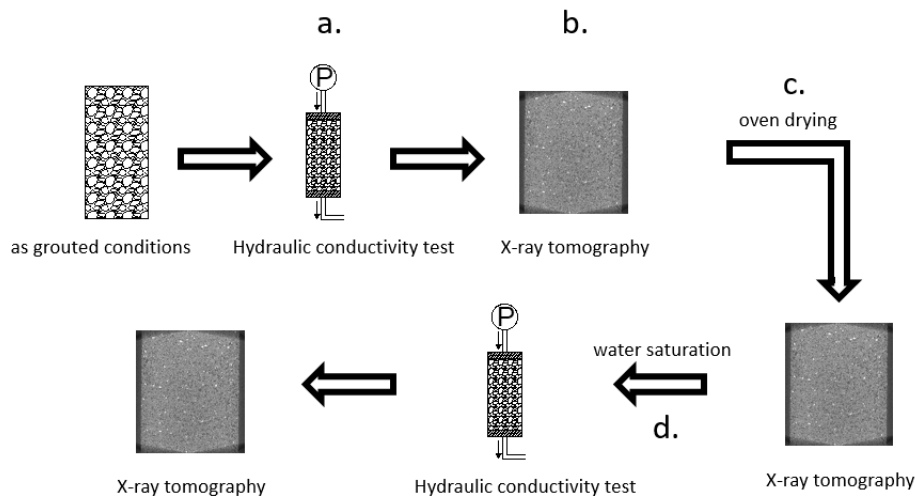


Figure 4. Experimental flow chart for hydraulic conductivity tests and x-ray tomography performed on grouted sand.

a. Hydraulic conductivity test. Hydraulic conductivity tests were performed by keeping the specimen in the same acrylic cylinder in which it was grouted. The acrylic cylinder was designed to fit the permeability apparatus that was used to measure the hydraulic conductivity. At the bottom of the cell the specimen was in contact with a porous stone and at the top the specimen was secured by means of a perforated metallic disc, to provide drainage. Water flow was forced from the top to the bottom of the specimen. Water pressure was applied by means a GDS ADVPC pressure-volume controller. The pump provided automated readings of both the applied pressure and change in water volume at any given time. The hydraulic conductivity test was conducted at 20 kPa of water pressure, giving a hydraulic gradient of about 13.5. The final water pressure was achieved by increasing the pressure in three steps (5 kPa, 10kPa and 20kPa) over a period of 1 hour. Once the final pressure was achieved, it was kept constant for 5 hours and the flow rate through the sample was recorded. Steady state conditions were achieved within 2 hours.

b. X-ray tomography. X-ray tomographies of the sample were performed with a Nikon

XT H 320. The scans were performed at 183kV energy, 216 μ A current and 3141 projections were performed during a single revolution. The resulting resolution was of 0.0198 pixels per μ m and a voxel size of 50.4683x50.4683x62.8339 μ m. A copper filter 1mm thick was used. During the scan the cylinder was covered with parafilm® to maintain a constant water content.

c. Oven drying. The sample was oven-dried at 60°C for 48 hours.

d. Water saturation. Saturation after drying was performed in the hydraulic conductivity cell. A constant water pressure (20 kPa) was applied for 48h. At this pressure, the water flow achieved a constant rate only after approximately 32 hours. At this point the sample was considered to be saturated. The water pressure was then reduced to atmospheric pressure, and the specimen was left under water for another 24h. Following this, the hydraulic conductivity test was performed as explained above. The level of saturation achieved was assessed by measuring the air-pore space with the subsequent X-ray scan, which was found to be negligible.

Additional hydraulic tests

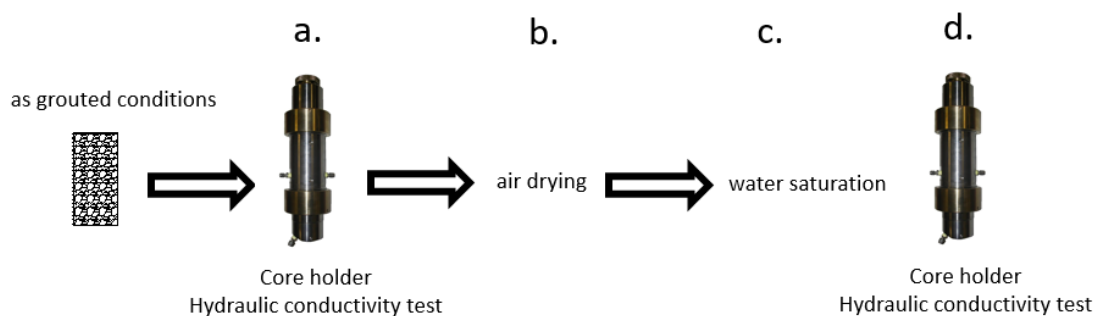


Figure 5. Experimental flow chart for hydraulic conductivity tests by means of core holder

Hydraulic conductivity tests after a drying and wetting cycle were also conducted on a

sample of a smaller volume (inner diameter 38 mm) within a core holder set-up to enable a lateral confining pressure of 1500kPa to be applied in order to avoid water by-pass around the specimen (Figure 5).

- a. In “as grouted” condition hydraulic conductivity was tested as follows. A confining lateral pressure of 1500 kPa was applied for 24 hours. Successive, increments in injection pressure at the inlet were applied for approximately 60 hours per step. The injection pressure steps were: 50 kPa, 100 kPa, 200 kPa, 400 kPa, 200 kPa, 100 kPa and 50 kPa.
- b. The sample was tested both in the “as grouted condition” and after one drying and wetting cycle. For this sample, the drying stage was not carried out in the oven, but consisted of 14 days in the open air at room temperature. It is worth noting that on such a small sample oven drying was not possible as the sample became too fragile to sustain the operational handling, and broke repeatedly.
- c. For re-wetting, water was initially introduced at the base of the sample via capillary rise and then by total sample submersion. This was then followed by 15 continuous days of water injection, before a final hydraulic test was performed. The final amount of trapped air was not measured as no X-ray scan was performed on this sample.
- d. Hydraulic conductivity of the sample after a complete drying-wetting cycle was carried out as follows. In the core holder, a confining pressure of 1500 kPa was applied until further displacement was no longer measurable. Two different injection pressures were then applied at the inlet in succession: 50 kPa and 100 kPa for approximately 20 hours each step.

Both for *a* and *d*, as the injected volume was recorded, the hydraulic conductivity was estimated by calculating the average injection rate over each 10 minute period.

6. IMAGE PROCESSING

For each x-ray tomography scan the centre of rotation, beam hardening correction and 3D reconstruction was performed with Nikon' software Nikon's CT Pro 3D. For the image-processing the open source software FIJI (Schindelin et al., 2012) was used. For all the image sequences, a 3D Gaussian blur was used in order to reduce the noise. A standard deviation of 2 was applied in all three directions. Such a filter was proven to be sufficient to reduce the noise and enable the subsequent image analysis.

Region of interest

A study on the required dimension of the region of interest (ROI) was performed by computing the porosity of centred volumes of different dimensions.

Each 3D volume was thresholded with the same grey value and transformed into a sequence of binary images. The porosity of each volume was then computed with a dedicated function. In Figure 6a and Figure 6b a vertical cross section and a horizontal cross section of the specimen are presented respectively along with some of the studied ROIs. In Figure 6c the calculated porosity (normalized with the maximum calculated porosity) is reported for different cube volumes. The smallest volume investigated was a cube with a side of 125 pixels (dotted line in Figure 6) and the largest a cube with a side of 1100 pixels (solid line in Figure 6). As expected, the normalized porosity changes significantly when the considered volume is small. As the volume size increases, the normalized porosity achieves a constant value. As ROI, the volume of a cube having 1100 pixel side (corresponding to a volume of $1.33 \cdot 10^9$ voxels) was selected.

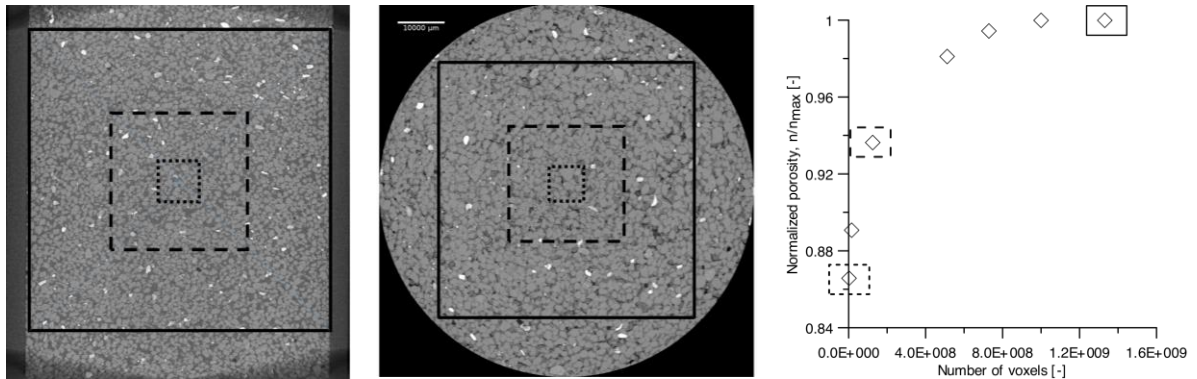


Figure 6. Study on the ROI dimension. a) specimen cross section (vertical), b) specimen cross-section (horizontal) and ROI representation, c) normalized porosity vs number of voxels per ROI.

Segmentation

For each image sequence, three different phases were encountered: sand, CS grout and air.

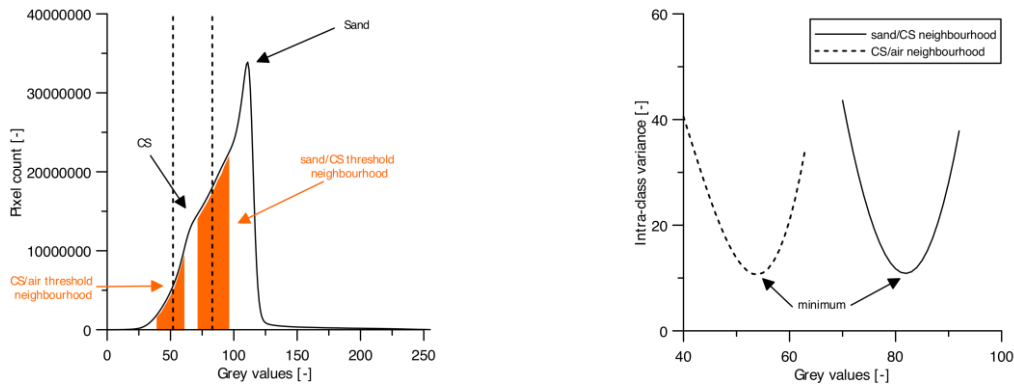


Figure 7. Thresholding. a) Grey values histogram, b) intra-class variance

In Figure 7a the histogram of the grey value frequency is reported. The histogram presents one well defined peak, associated with the sand grains, and a well-defined change in slope,

associated with the CS, no critical points could be associated to the third phase (air). Furthermore, no significant changes on the histogram function were present so that global threshold detection methods, such as e.g. Otsu's method (Otsu, 1979), mean method (Glasbey, 1993) or minimum method (Prewitt and Mendelsohn, 1966), could be applied.

For each phase transition, a neighbourhood of grey values was defined by visual inspection of the images, such that the phase transition occurred within the selected range. In the same way that Otsu's method uses the global histogram, a similar algorithm was applied within each of the defined neighbourhoods. Within each neighbourhood a threshold value outlining two classes was defined. The threshold value was then optimised as the value minimising the intra-class variance. Figure 7b represents the intra-class variance for the two neighbourhoods as the threshold value was changed.

A sensitivity analysis on the thresholding method was conducted by comparing the experimentally determined porosity (of the pre-grouted sand) with the total porosity that was computed for a range of grey values, which were centered around the selected sand/CS threshold (Figure 8). The difference between the experimental porosity and the calculated one is minimal for the threshold value determined from Figure 7b.

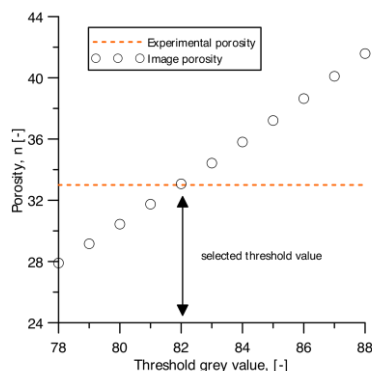


Figure 8. Sensitivity analysis on the threshold value selection

Pore size distribution

For each image sequence, the pore space 3D discretization in different classes and the computation of the volume associated to each class was performed using a FIJI plugin: “Beat”, which implements the algorithm described in Münch and Holzer (2008). In order to divide the pore space into a given number of subregions, a 3D “distance map” is calculated, indicating the distance of each pixel to the closest boundary. By selecting the contour lines the required subregions are then isolated. For each subregion the associated volume is then calculated. This method, a so called “continuous Pore Size Distribution” has been preferred over the more simplistic method where the size of each pore (regardless its shape) is simply calculated as the diameter of the sphere having an equivalent volume. The latter method, generally yields a bigger breakthrough value and a more scattered pore size distribution (a detail discussion is given in Münch and Holzer (2008)).

In order to study the connectivity of the voids, the volume of each class of pores was also computed by simulating mercury intrusion porosimetry (MIP) (i.e. the intrusion of a non-wetting fluid into the pore structure). “Beat” simulates the process of mercury intrusion into a pore network by means of a “region-growing algorithm” (Münch and Holzer, 2008) that includes a constraint in the sense that a new pixel is only allowed to join a region if it meets the growing criterion. In the case of MIP analysis the selected growing criterion is the well-known Washburn equation (Washburn, 1921). As shown by Washburn equation (equation [1]) the relation between the diameter of the intruded pores, d , and the applied pressure, ΔP , is described by two different parameters: surface tension, γ , and contact angle, θ .

$$d = - \frac{4 \cdot \gamma \cdot \cos\theta}{\Delta P} \quad [1]$$

As mercury intrusion is simulated from an external boundary, only the pores connected via a continuous path to this boundary are intruded. Therefore, this analysis, represents an indirect method of measuring pore space connectivity.

From all of the obtained cumulative pore distributions, the pore size distribution (PSD) was calculated with a dedicated algorithm, which calculates the difference quotient for a given number of intervals equispaced on a log scale.

7. EXPERIMENTAL RESULTS

Water retention curve

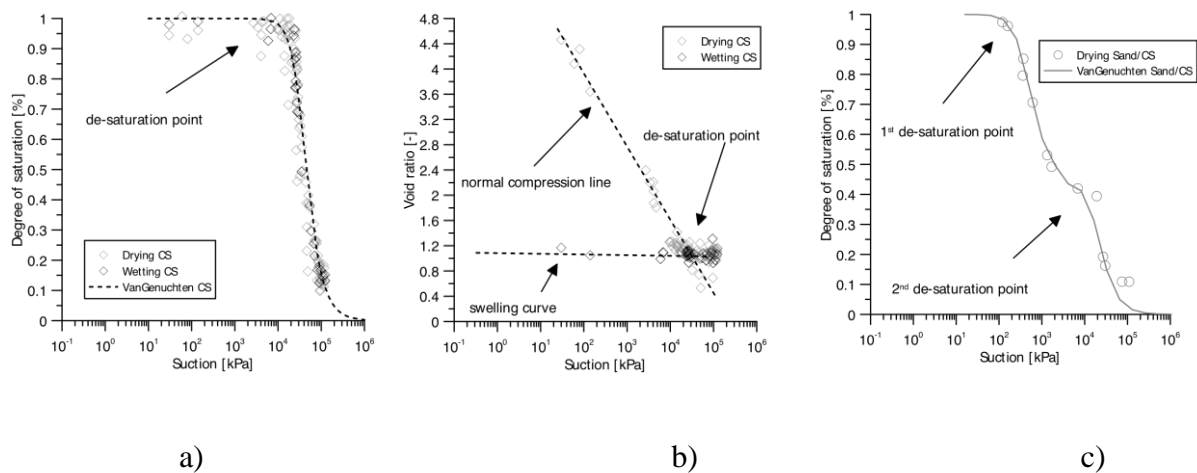


Figure 9. Water retention curve. a) Colloidal silica water retention curve in terms of degree of saturation, b) Colloidal silica water retention curve in terms of void ratio and c) sand grouted with colloidal silica water retention curve in terms of degree of saturation.

The water retention curve of specimens of CS are reported in Figure 9a and Figure 9b in terms of degree of saturation and void ratio respectively. Both the main wetting and the main drying path have been investigated, for a range of suction values from 100 kPa to 120000 kPa. The water retention curve shows CS to have an air-entry value of about 24000 kPa and achieves full

desaturation only at suction values above 120000 kPa. Both the drying and the wetting data lie on the same curve, that is to say there is no hydraulic hysteresis. In order to ease later comparison, a Van Genuchten curve fitting the experimental data is also reported (Van Genuchten, 1980). Figure 9b presents the void ratio of CS specimens along the same drying and wetting path. The void ratio along the drying path (increasing suction) shows a logarithmic trend before de-saturation occurs (suction values less than 120000kPa). The change in void ratio occurring before desaturation is generally associated with the normal compression curve of the material as the suction induced on drying controls the effective stress of the specimen in the saturated state (Tarantino, 2010). This is indeed linear when plotted in a semi logarithmic space. Once desaturation begins, the void ratio trend changes and further volume change is limited. On wetting (i.e. reduction in suction), the data is again linear in a semi logarithmic space along the whole range of investigated suction values (swelling curve in Figure 9b). It is worth noting that the wetting causes only a limited swelling of the sample, corroborating the experimental results presented in Wong et al. (2018) where the reduced CS elastic potential was already noted. This minimal change in volume on wetting is partly responsible for the lack of hydraulic hysteresis between the drying and wetting curves. This is in addition to the uniformity of the particles and therefore the pores which means that there is no significant ink-bottle effect typically found in soils (Haines, 1930).

In Figure 9c, the water retention curve of a sand grouted with CS is reported in terms of degree of saturation. The obtained curve presents a bi-modal trend with two inflection points. The first de-saturation point occurs at about 200kPa, whereas the second at about 20000 kPa. As in the case of CS only, full de-saturation occurs for suction values above 120000 kPa. Also in this case, the data have been fitted with a bi-modal Van Genuchten curve.

SEM analyses

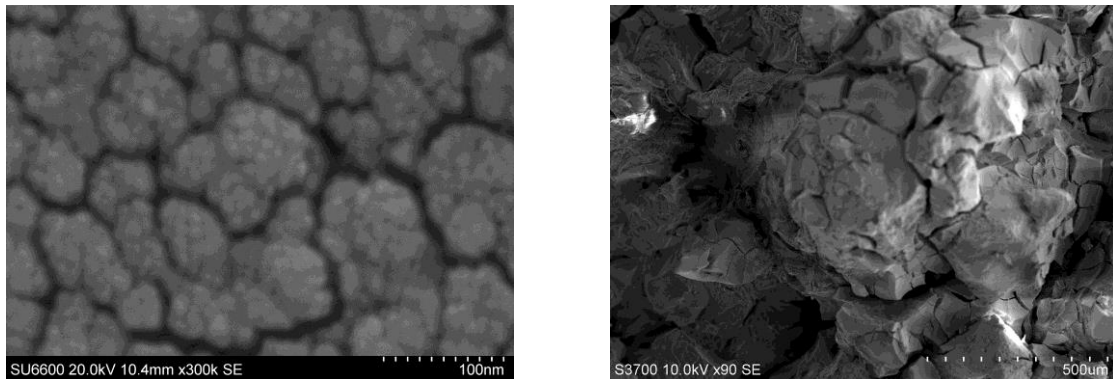


Figure 10. SEM images of a) oven dried CS and b) oven dried sand grouted with CS.

In Figure 10a and Figure 10b the SEM images of an oven dried specimen of CS and an oven dried sample of sand grouted with CS are shown respectively. Figure 10a (magnification factor of 300k) shows the SEM image of a specimen of CS with a full scale of about 500 nanometres. At this scale, single CS particles are visible. It appears evident, that individual particles tend to aggregate in bigger clusters of tens of particles. A continuous network of nano-cracks of the order of tens of nanometres wide are detectable among the CS clusters.

Figure 10b (magnification factor of 90) shows the SEM image of a specimen of sand grouted with CS with a full scale of about 1.5 mm. The sand particles are not visible and they appear to be completely surrounded and covered by a continuous matrix of CS. At this scale the CS particles, CS clusters and the nano-cracks are no longer visible. However, desiccation cracks (meso-cracks) in the order of hundreds of microns wide are detectable on the CS surface.

X-ray tomography and PSD

X-ray images of a specimen of grouted sand in the “as grouted” condition and after a drying and wetting cycle are shown in Figure 11a and Figure 11b respectively. As already shown in

the SEM image (Figure 10b) the CS surrounds the sand grains filling all the available void space. By comparing Figure 11a and Figure 11b it is possible to notice that meso-cracks (air voids) are formed in the CS matrix as a consequence of the drying-wetting cycle. This was observed to be the case throughout the specimen. Also at this scale, the resolution of the X-ray scans is not sufficient to enable the nano-cracks and the CS particles to be seen as was observed in Figure 10a.

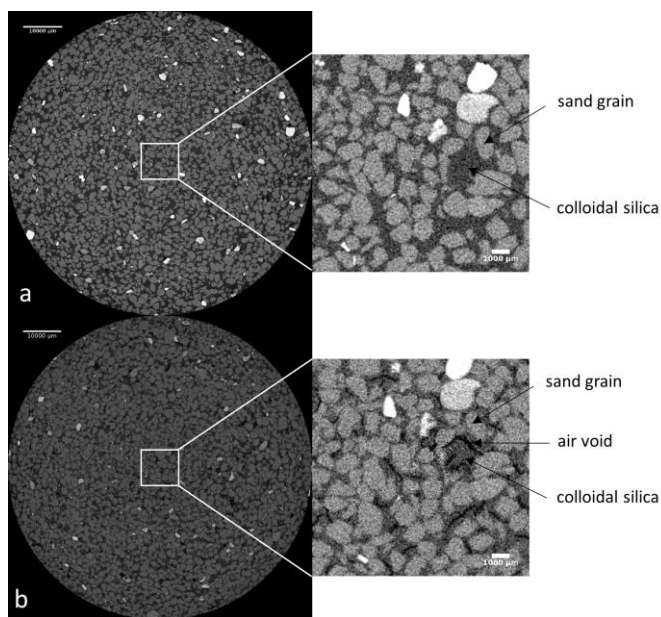


Figure 11. X-ray images of grouted sand. a) as grouted conditions and b) after a drying and wetting cycle.

In Figure 11b three different phases are discernible: sand, CS and air. In order to study the evolution of PSD within a grouted sample and to discern the deformation of the sand skeleton, the CS matrix and the cracks, the void space was divided in to three different classes: i) the void space within the sample that is not occupied by the sand grains (all available pore space), ii) the pore space that is occupied by CS and iii) the pore space that is filled by air (cracks). According to this classification, the sum of the crack pore volume and the CS pore volume must equal the

total available pore space. In Figure 12 it is shown how for a given image of grouted sand (Figure 12a), the three classes (Figure 12b, Figure 12c and Figure 12d) have been detected according to the criteria described.

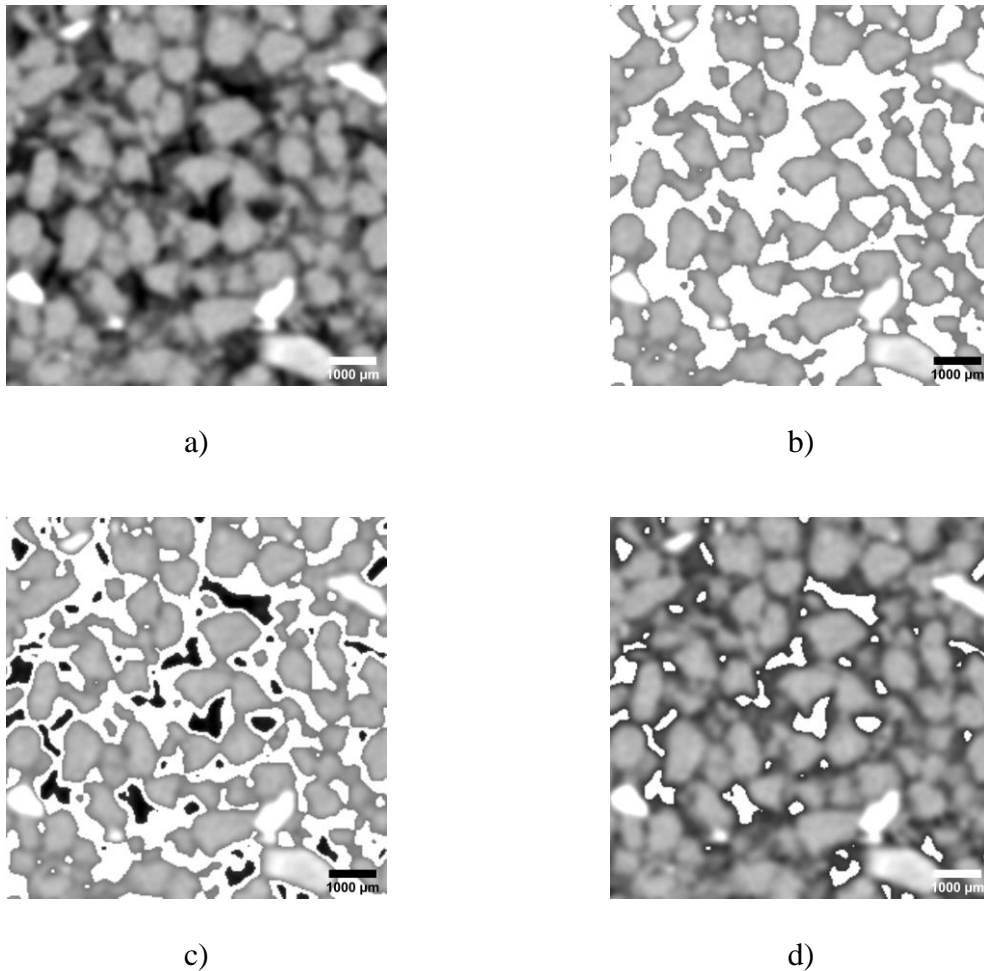


Figure 12. Pore space classification. a) X-ray image, b) available pore space (shown in white), c) pore space filled by CS (shown in white) and d) pore space filled by air (shown in white).

X-ray scanning was performed on the same specimen at three different stages: (i) as grouted, (ii) after a drying stage and (iii) after the subsequent wetting stage. The evolution of the porosity associated with each of the three classes of pores at each of these three stages is reported in Figure 13. In Figure 13a, Figure 13c and Figure 13e the cumulative pore distribution is reported. For each class the porosity was defined as the ratio between the volume of pores

associated to the given class and the total volume of the specimen. In Figure 13b, Figure 13d and Figure 13f the PSD in terms of porosity frequency is reported.

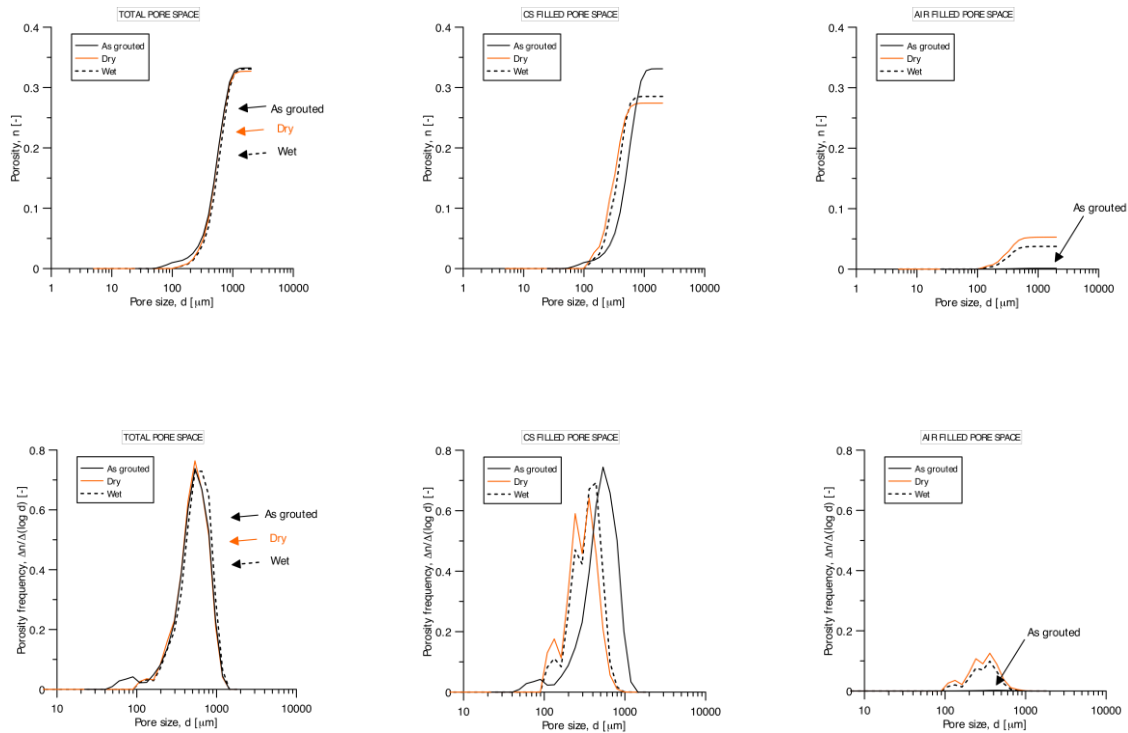


Figure 13. Pore distribution of a sample of sand grouted with CS. a) Cumulative pore distribution of the pore space, b) PSD of the pore space, c) cumulative pore distribution of pores filled by CS, d) PSD of pores filled by CS, e) cumulative pore distribution of dry pores and f) PSD of dry pores.

Upon the drying and wetting cycle, the sand skeleton does not appear to undergo any volume change. Indeed both the cumulative pore distribution (Figure 13a) and the PSD (Figure 13b) of the total available pore space does not change from the “as grouted” condition to the dry and the wet conditions. The initial (and final) porosity of the sample is indeed 0.331 as was determined experimentally) and the dominant modal value of the PSD remains 0.535 μm at

each stage.

On the other hand, it is clear that the pore space occupied by CS reduces upon drying (Figure 13c). The porosity changes from 0.331 for the “as grouted” condition to 0.275 after following the drying path. Upon wetting the volume associated with the CS filled pores increases slightly to 0.285, indicating some swelling of the CS grout. Accordingly, the dominant mode of the PSD of the CS filled pores (Figure 13d) reduces upon drying from 0.535 μm to 0.295 μm . Upon the subsequent wetting stage a small increase in the dominant modal value is also detected.

On the other hand the evolution of the air filled pore space increases to 0.053 upon drying from initially being close to zero under ‘as-grouted conditions’ (arrow in Figure 13e), indicating the formation of cracks. Upon wetting the air filled pore space reduces slightly to 0.037 as a consequence of the limited amount of CS swelling (Figure 13e). The PSD of this class (Figure 13f) shows a modal value of 0.295 μm both after the drying and the wetting path.

In Figure 14, for each pixel of the pore space filled by CS, the Euclidean distance to the nearest sand grain boundary is represented for a 2D cross-section of the specimen (Kimmel and Bruckstein, 1993, Kimmel et al., 1996, Münch and Holzer, 2008). In Figure 14a the Euclidean map of a fraction of the specimen of sand grouted with CS is shown. The sand grains are represented in grey. The distance to the nearest boundary is indicated by the colour of the pore space, with blue being the shortest distance and red being the greatest distance to the nearest grain boundary. In Figure 14b, the same 2D cross-section of the specimen is presented after drying. The voids filled with air have been superimposed on to the Euclidean map in white. It is worth noting how the air porosity (i.e. cracks) appear at the centre of the larger pores (white marks in Figure 14b).

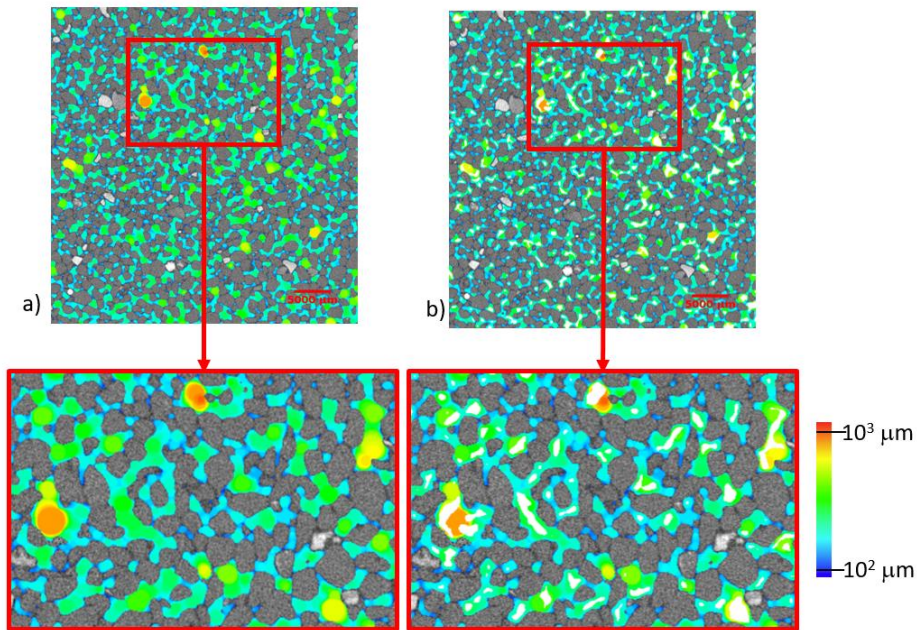


Figure 14. Pore space Euclidean distance map of sand grouted with CS in a) as grouted condition and b) dry conditions.

Finally, in order to investigate the degree of connectivity between the cracks formed upon drying, the cumulative pore distribution of air filled porosity was computed with the so-called “*continuous PSD*” method (*Air* in Figure 15) is compared with the PSD calculated with the so-called “*MIP PSD*” method (*Connected Air* in Figure 15). As previously discussed, the latter method simulates the PSD that would be determined based on mercury intrusion. By simulating the MIP test, only the volume of the pores connected via a continuous path to an external boundary are taken into account. Despite the formation of cracks upon drying, Figure 15 highlights that these cracks do not form a continuous connected network of voids. Indeed the simulated volume of the connected porosity results are negligible compared to the cumulative porosity of the actual continuous PSD.

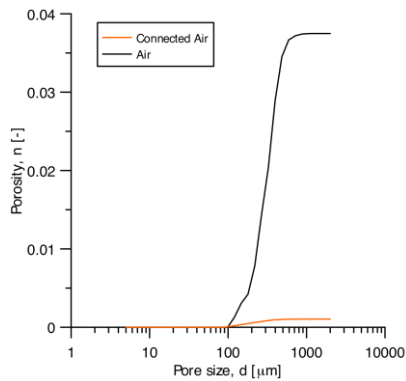


Figure 15. Cumulative pore distribution of the pore space filled by air of a sample of sand grouted with CS after drying. Comparison between total air porosity and connected air porosity.

Hydraulic conductivity measurement

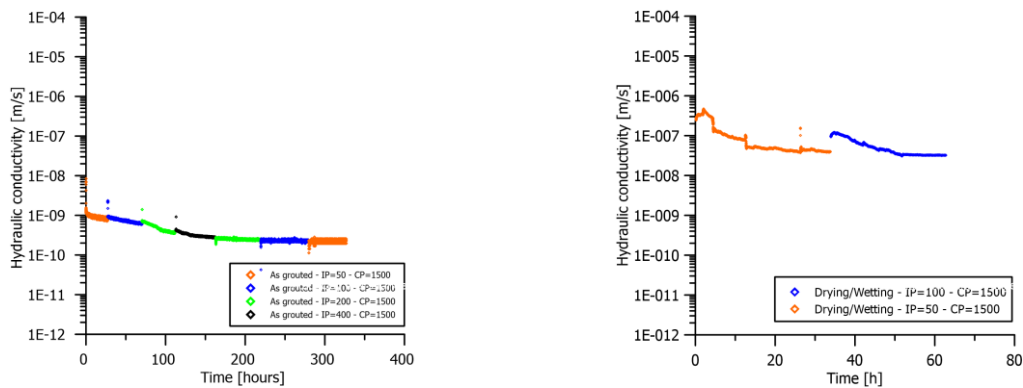


Figure 16. Results of the core holder hydraulic conductivity test. a) Hydraulic conductivity of the sample in “as grouted” conditions and b) hydraulic conductivity of the sample after one cycle of drying and wetting.

Figure 16 shows the results of the hydraulic conductivity tests carried out by means of a core holder, within which it was possible to apply a confining pressure (CP) of 1500 kPa to inhibit bypass flow. Figure 16a shows the results of the test carried out on the sample in “as grouted” conditions. Figure 16b the hydraulic conductivity of the sample after one cycle of drying and subsequent wetting.

Under ‘as-grouted’ conditions, the hydraulic conductivity at the beginning of the test is at approximately $1 \cdot 10^{-9}$ m/s. During the test the hydraulic conductivity decreases until 200 hours and stabilises to a value of $2 \cdot 10^{-10}$ m/s, almost one order of magnitude lower. The hydraulic conductivity of the sample after one drying and wetting cycle was measured to be approximately $3 \cdot 10^{-8}$ m/s

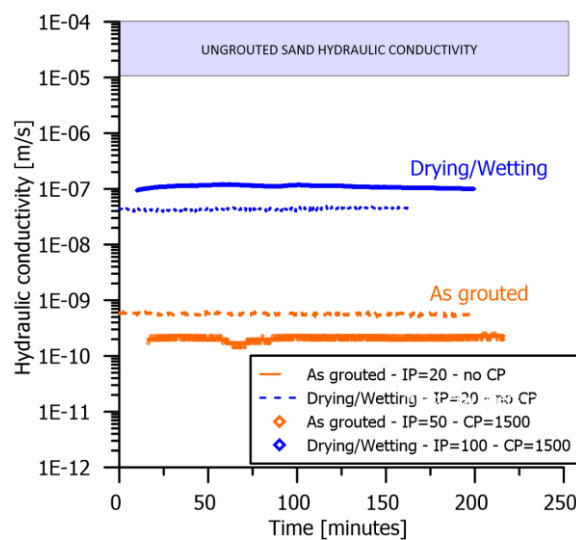


Figure 17. Hydraulic conductivity test on grouted sand, before and after a drying and wetting cycle.

For comparison with Figure 16, Figure 17 shows the results of hydraulic conductivity tests in which no confining pressure was applied (“no CP” in the figure). Under ‘as-grouted’ conditions, the hydraulic conductivity is approximately $5 \cdot 10^{-10}$ m/s. After a complete cycle of drying and wetting (which included oven drying at 60°C for 48 hrs) the hydraulic conductivity increased by 2 orders of magnitude, to a value of approximately $5 \cdot 10^{-8}$ m/s.

8. DISCUSSION

In Figure 17, the hydraulic conductivity of the grouted sand sample before and after severe drying is compared. In the same figure, the range of hydraulic conductivity for ungrouted sand is also reported. It is shown that after severe drying, although the hydraulic conductivity increases by two orders of magnitude, the hydraulic conductivity of the grouted sand sample is still at least three orders of magnitude smaller than the initial hydraulic conductivity of the sand sample prior to colloidal silica grouting.

The hydraulic conductivity tests carried out with and without confining pressure show similar results. This is perhaps to be expected as during the preparation of the sample for the hydraulic conductivity test, where no confining pressure was provided, the sand was grouted directly in the mould, so it appears that the CS bond with the acrylic mould was sufficient to avoid flow by-pass around the specimen.

It is worth noting that the hydraulic conductivity in the test reported in Figure 16a dropped by approximately one order of magnitude during the test. Although further investigation is required, the drop in hydraulic conductivity may result from a reduction in the osmotic potential in the CS. As NaCl was used as an accelerator during the grout mixing, the grout has a Na concentration of 0.28 M. As fresh water was injected into the sample during the hydraulic conductivity test, the Na concentration could therefore decrease resulting in a corresponding decrease in the osmotic pressure and could induce an associated swelling.

The sketch shown in Figure 18 highlights the cracking mechanisms inferred from the experimental campaign presented here. As shown by the SEM image in Figure 10a, the CS matrix is made by a network of clusters of tens of silica particles (Figure 18c). As the CS dries,

nanoscale cracks appear between the clusters (Figure 18d). Such cracks are approximately 10 nm wide.

Likewise, the water retention curve presented in Figure 9a, showed the air-entry value of the CS to be approximately 24000kPa. To estimate an order of magnitude of the pore size corresponding to this suction value, in the first instance, one can assume the water-CS contact angle to be equal to 0° and hence calculate the corresponding pore diameter by means of the Washburn equation. In this case, the pore size corresponding to an air-entry value of 240000 kPa is 12nm, which is in excellent agreement with the SEM picture shown in Figure 10a. This observation corroborates the hypothesis that when colloidal silica dries in an unrestrained environment, cracks only form at the nano-scale, thus guaranteeing a high retention capacity and a low hydraulic conductivity.

By contrast, when CS dries whilst being restrained by the surrounding sand skeleton, as in the SEM image of Figure 10b and by the X-ray CT analysis (Figure 11, Figure 12, Figure 13 and Figure 14) cracks hundreds of microns in width appear. It is thought that the severe shrinkage that CS undergoes when drying induces an increase in tensile stress, with crack generation occurring once the tensile strength of the material is reached. This is the same mechanism that has been suggested to be responsible for desiccation cracking in clay liners by Kleppe and Olson (1985). As shown in Figure 9b, upon a main drying path, CS volumetric shrinkage is about 60%. Thanks to the boundary provided by the sand skeleton, during drying the increase in tensile stress within a CS filled pore results in the formation of a crack at the centre of each pore, where the strain is the highest (Figure 18e). The meso-scale cracks are responsible for the additional and reduced air-entry value displayed by the grouted sand when compared to the CS only.

In Figure 19a, the water retention curve of the grouted sand (previously showed in Figure

9c) is compared to the water retention curve of both a pure sand (not grouted) with a similar particle size distribution to the sand used in this study (Burger and Shackelford, 2001) and to a water retention curve for CS only (previously showed in Figure 9a). The water retention curve of the ungrouted sand generally presents very low air-entry values (several Pascal) and desaturates within a very small suction range (several kPa). On grouting, the air-entry value increases by 3-4 orders of magnitude, as does the water retention capacity. Due to the presence of the two cracking modes described above, the water retention curve for grouted sand is bi-modal. The smallest air-entry value (at ~200kPa) can be associated to the mesoscale cracks occurring at the centre of the sand pores. The second air-entry value (at ~20000kPa) can be associated to the same mechanism that controls desaturation in the CS only, i.e. nanoscale cracks occurring at the silica cluster scale.

In Figure 19b, the water retention curve of the grouted sand is compared with the water retention curve of a consolidated kaolin (Tarantino, 2009) and to a geosynthetic bentonite clay liner, Bentofix NSTM (Southen and Rowe, 2007). Even though the initial material was a loose sand, it is clear that grouting with CS enhanced the water retention capability of the sand to such an extent that it became similar to that of a bentonite geosynthetic and a consolidated kaolin clay.

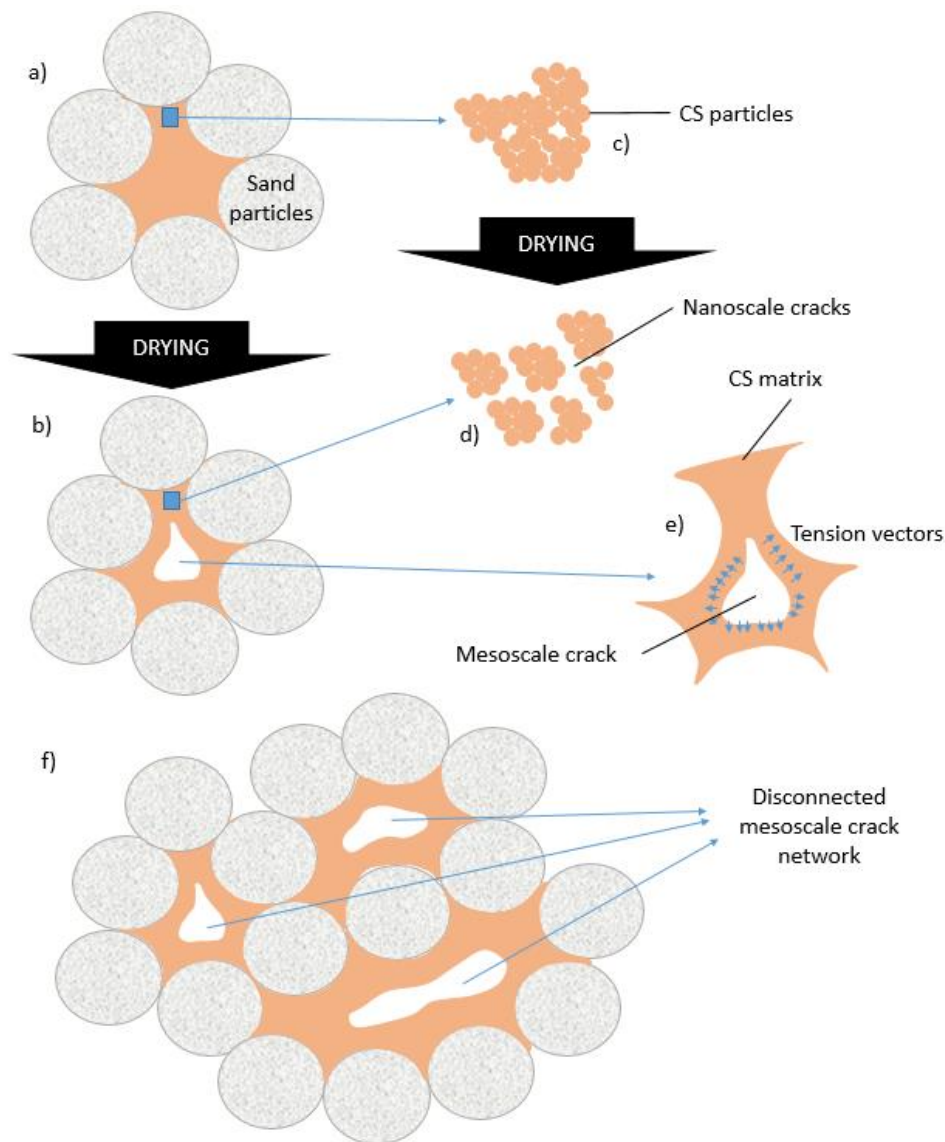


Figure 18. Cracking mechanisms. a) CS particle arrangement, b) CS nanocracks, c) CS mesoscale cracks, d) pore configuration within sand grouted with CS, e) mesoscale cracks within a pore in grouted sand and f) disconnected mesoscale crack network in grouted sand.

In terms of volumetric behaviour, CS is shown to be very deformable along the main drying curve (Figure 9b), whereas along the wetting curve little change in total volume occurred (Figure 9b). This limited elastic swelling is also corroborated by the PSDs showed in Figure 13c, Figure 13d, Figure 13e and Figure 13f. According to this experimental evidence one could hypothesise that once cracks are formed along the main drying path, little volume change will

occur during subsequent wetting/drying cycles, as most of the CS deformation has already occurred. Furthermore, when the grouted sample is saturated the sand skeleton provides the CS with a rigid boundary. On the other hand, once cracks have formed, the CS becomes less restrained and therefore the risk of additional cracking is less probable.

As a purely theoretical disquisition, it is worth noting that an approximate air-entry value of 24000kPa for the CS corresponds to a capillary rise potential of 2.4 km. This implies that, as long as a continuous network of CS is in hydraulic contact with the water table, a theoretical capillary rise of 2.4 km is achievable and that the CS will not desaturate. However, due to the rigid sand skeleton, experiments show that the initial air-entry value drops to about 200kPa when the tensile strength of the silica is exceeded in the centre of a pore upon CS shrinkage. An air-entry value of approximately 200kPa corresponds to a potential capillary rise of approximately 20 m. These results suggest that in temperate regions, where the water table is generally < 20m below ground surface, as long as the barrier (or temporary works) is engineered to intersect the water table, the CS-grouted sand will not crack and the barrier will remain pristine. It is also worth noting that pure coarse sand is a worst-case scenario in terms of providing a rigid boundary and that the presence of finer soil (i.e. fine sand or silt) will increase the shrinkage capability of the material upon drying resulting in a higher initial air-entry value.

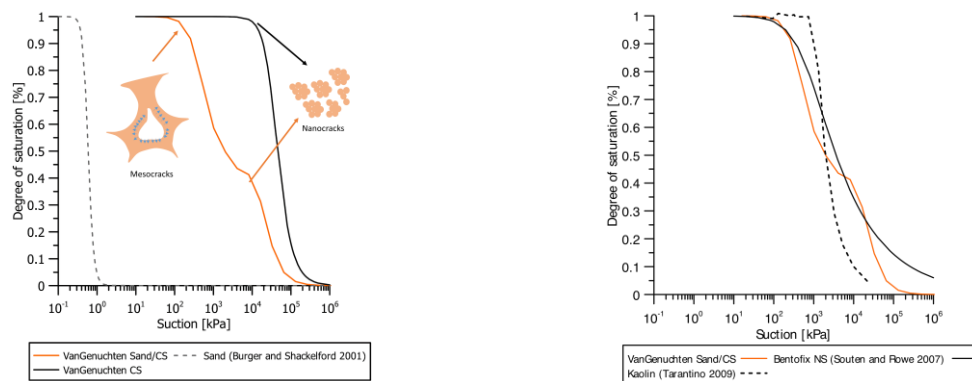


Figure 19. Grouted sand water retention curve comparison. a) comparison with ungrouted sand and CS only and b) comparison with kaolin clay and Bentofix NS geotextile.

9. CONCLUSIONS

This paper investigates the potential for using the injection of colloidal silica grout for the creation of low hydraulic conductivity barriers for use in nuclear decommissioning. The advantage of CS over traditional barrier installation methods, such as bentonite slurry walls or cement jet grouting, is its capability to permeate into in situ soils under low injection pressures, to be injected beneath regions of existing contamination, and that no excavation of any hazardous material is required.

In order to understand the benefits and the drawbacks associated with the use of colloidal silica grout in near surface applications, where drying and wetting patterns may pose a severe risk to barrier integrity, a microstructural study was carried out on the mechanism of cracking of colloidal silica injected within a rigid sand lattice. This study has shown that:

- Sand grouted with CS exhibits a bi-modal water retention curve and its hydraulic conductivity lies within a range similar to that of commercially available clay barrier

materials.

- On drying, nanoscale cracks form within the CS matrix, which are 10s of nanometres in width. These have an associated air-entry value of ~20,000-24,000kPa,
- Additional meso-scale cracks can also form in CS filled pores when surrounded by sand grains, due to conditions of restrained shrinkage. These cracks are typically hundreds of microns in width and have an associated air-entry value of ~200kPa.
- The CS grouted sand exhibited a saturated hydraulic conductivity of $5 \cdot 10^{-10}$ m/s. Even after being exposed to severe drying conditions (more extreme than would be encountered in field conditions) the CS grouted sand still exhibited a saturated hydraulic conductivity of $5 \cdot 10^{-8}$ m/s, still at least 3 orders of magnitude lower than the original hydraulic conductivity of the ungrouted sand.
- Analysis of the connectivity of the pore space filled by air after drying indicates that although cracks form, a connected network does not, thus explaining the observation that even after severe drying the CS grouted sand retains a very low hydraulic conductivity.

Despite the elevated initial porosity of the sand sample and the severe oven drying conditions imposed, the colloidal silica grout results in a reduction in hydraulic conductivity of at least 3 orders of magnitude, when compared to the initial hydraulic conductivity of the ungrouted sample. Hence, although in the worst-case scenario of oven-drying a CS-grouted sand, the final hydraulic conductivity is higher than the desired threshold of 10^{-9} m/s for a hydraulic barrier (for example for use in landfills), the treatment with colloidal silica would still greatly limit the migration of in-situ contaminants. This material shows great potential for use as an injectable hydraulic barrier, particularly on nuclear decommissioning sites where the presence of existing

contaminated material or the fragility of neighbouring structures restricts the use of other more invasive techniques for creating hydraulic barriers.

10. ACKNOWLEDGEMENTS

The authors gratefully acknowledge the financial support of the Research Councils' UK Energy Programme under grant EP/L014041/1, Decommissioning, Immobilisation and Storage Solutions for Nuclear Waste Inventories (DISTINCTIVE). All data underpinning this publication are openly available from the University of Strathclyde KnowledgeBase at [10.15129/06540872-c30f-45c8-93fc-a2bfd524e944](https://doi.org/10.15129/06540872-c30f-45c8-93fc-a2bfd524e944).

11. REFERENCES

- ALBRECHT, B. A. & BENSON, C. H. 2001. Effect of desiccation on compacted natural clays. *Journal of Geotechnical and Geoenvironmental Engineering*, 127, 67-75.
- ALBRIGHT, W. H., BENSON, C. H., GEE, G. W., ABICHO, T., TYLER, S. W. & ROCK, S. A. 2006. Field performance of three compacted clay landfill covers. *Vadose Zone Journal*, 5, 1157-1171.
- AXELSSON, M. 2006. Mechanical tests on a new non-cementitious grout, silica sol: A laboratory study of the material characteristics. *Tunnelling and underground space technology*, 21, 554-560.
- BAHADUR, A., HOLTER, K. & PENGELLY, A. Cost-effective pre-injection with rapid hardening microcement and colloidal silica for water ingress reduction and stabilisation of adverse conditions in a headrace tunnel. *Underground Space–The 4th Dimension of Metropolises, Three Volume Set+ CD-ROM: Proceedings of the World Tunnel Congress 2007 and 33rd ITA/AITES Annual General Assembly, Prague, May 2007, 2007. CRC Press, 297.*
- BOYNTON, S. S. & DANIEL, D. E. 1985. Hydraulic conductivity tests on compacted clay. *Journal of Geotechnical Engineering*, 111, 465-478.
- BURGER, C. A. & SHACKELFORD, C. D. 2001. Evaluating dual porosity of pelletized diatomaceous earth using bimodal soil-water characteristic curve functions. *Canadian Geotechnical Journal*, 38, 53-66.
- BUTRÓN, C., AXELSSON, M. & GUSTAFSON, G. 2009. Silica sol for rock grouting: Laboratory testing of strength, fracture behaviour and hydraulic conductivity. *Tunnelling and underground space technology*, 24, 603-607.
- BUTRÓN, C., GUSTAFSON, G., FRANSSON, Å. & FUNEHAG, J. 2010. Drip sealing of tunnels in hard rock: A new concept for the design and evaluation of permeation grouting. *Tunnelling and underground space technology*, 25, 114-121.
- CHANGIZI, F. & HADDAD, A. 2017. Improving the geotechnical properties of soft clay with nano-silica particles. *Proceedings of the Institution of Civil Engineers-Ground Improvement*, 170, 62-71.
- COBOS, D. R. & CHAMBERS, C. 2010. Calibrating ECH2O soil moisture sensors. *Application Note, Decagon Devices, Pullman, WA.*
- COSTA, S., KODIKARA, J. & SHANNON, B. 2013. Salient factors controlling desiccation cracking of clay in laboratory experiments. *Geotechnique*, 63, 18.
- GALLAGHER, P. M., CONLEE, C. T. & ROLLINS, K. M. 2007. Full-scale field testing of colloidal silica grouting for mitigation of liquefaction risk. *Journal of Geotechnical and Geoenvironmental Engineering*, 133, 186-196.
- GALLAGHER, P. M. & MITCHELL, J. K. 2002. Influence of colloidal silica grout on liquefaction potential and cyclic undrained behavior of loose sand. *Soil Dynamics and Earthquake Engineering*, 22, 1017-1026.
- GALLAGHER, P. M., SPATARI, S. & CUCURA, J. 2013. Hybrid life cycle assessment comparison of colloidal silica and cement grouted soil barrier remediation technologies. *Journal of hazardous materials*, 250, 421-430.
- GLASBEY, C. A. 1993. An analysis of histogram-based thresholding algorithms. *CVGIP: Graphical models and image processing*, 55, 532-537.

- GREEN, J. 2017. Half of the world's nuclear power industry is in crisis. *Chain Reaction*, 24.
- HAKEM, N., AL MAHAMID, I., APPS, J. & MORIDIS, G. Sorption of cesium and strontium on Savannah River soils impregnated with colloidal silica. International Containment Technology Conference, 1997. Petersburg:[sn], 652-657.
- HE, J., WANG, Y., LI, Y. & RUAN, X.-C. 2015. Effects of leachate infiltration and desiccation cracks on hydraulic conductivity of compacted clay. *Water Science and Engineering*, 8, 151-157.
- HENKEN-MELLIES, W.-U. & SCHWEIZER, A. 2011. Long-term performance of landfill covers-results of lysimeter test fields in Bavaria (Germany). *Waste Management & Research*, 29, 59-68.
- HEWITT, P. & PHILIP, L. 1999. Problems of clay desiccation in composite lining systems. *Engineering Geology*, 53, 107-113.
- ILER, R. K. 1979. *The Chemistry of Silica: Solubility, Polymerization, Colloid and Surface Properties, and Biochemistry*, John Wiley & Sons.
- JURINAK, J. & SUMMERS, L. 1991. Oilfield applications of colloidal silica gel. *SPE production engineering*, 6, 406-412.
- KIMMEL, R. & BRUCKSTEIN, A. M. Subpixel distance maps and weighted distance transforms. SPIE's 1993 International Symposium on Optics, Imaging, and Instrumentation, 1993. International Society for Optics and Photonics, 259-268.
- KIMMEL, R., KIRYATI, N. & BRUCKSTEIN, A. M. 1996. Sub-pixel distance maps and weighted distance transforms. *Journal of Mathematical Imaging and Vision*, 6, 223-233.
- KLEPPE, J. H. & OLSON, R. E. 1985. Desiccation cracking of soil barriers. *Hydraulic barriers in soil and rock*. ASTM International.
- LI, J. H., LI, L., CHEN, R. & LI, D. Q. 2016. Cracking and vertical preferential flow through landfill clay liners. *Engineering Geology*, 206, 33-41.
- LIAO, H., HUANG, C. & CHAO, B. 2003. Liquefaction resistance of a colloid silica grouted sand. *Grouting and ground treatment*.
- MANCHESTER, K., ZALUSKI, M., NORTH-ABBOTT, M., TRUDNOWSKI, J., BICKFORD, J. & WRAITH, J. Grout selection and characterization in support of the colloidal silica barrier deployment at Brookhaven National Laboratory. Proc. 2001 International Contain. and Remed. Technol. Conf. and Exhib., 10-13 June, 2001. Orlando, FL, 2001.
- MEER, S. R. & BENSON, C. H. 2007. Hydraulic conductivity of geosynthetic clay liners exhumed from landfill final covers. *Journal of geotechnical and geoenvironmental engineering*, 133, 550-563.
- MOLLAMAHMUTOGLU, M. & YILMAZ, Y. 2010. Pre-and post-cyclic loading strength of silica-grouted sand. *Proceedings of the Institution of Civil Engineers-Geotechnical Engineering*, 163, 343-348.
- MORIDIS, G., JAMES, A. & OLDENBURG, C. 1996. Development of a design package for a viscous barrier at the Savannah River site. Lawrence Berkeley National Lab., CA (United States). Funding organisation: USDOE Office of Environmental Restoration and Waste Management, Washington, DC (United States).
- MORIDIS, G., PERSOFF, P., APPS, J., MYER, L., PRUESS, K. & YEN, P. 1995. A field test of permeation grouting in heterogeneous soils using a new generation of barrier liquids. *Committed To Results: Barriers for Long-Term Isolation*. ER, 95.

- MORIDIS, G. J., FINSTERLE, S. & HEISER, J. 1999. Evaluation of alternative designs for an injectable barrier at the Brookhaven National Laboratory Site, Long Island, New York. *Water Resources Research*, 35, 2937-2953.
- MULHOLLAND, C., EJOHWOMU, O. A. & CHAN, P. W. 2019. Spatial-temporal dynamics of social value: Lessons learnt from two UK nuclear decommissioning case studies. *Journal of Cleaner Production*, 237, 117677.
- MÜNCH, B. & HOLZER, L. 2008. Contradicting geometrical concepts in pore size analysis attained with electron microscopy and mercury intrusion. *Journal of the American Ceramic Society*, 91, 4059-4067.
- OMIDI, G., THOMAS, J. & BROWN, K. 1996. Effect of desiccation cracking on the hydraulic conductivity of a compacted clay liner. *Water, Air, & Soil Pollution*, 89, 91-103.
- OTSU, N. 1979. A threshold selection method from gray-level histograms. *IEEE transactions on systems, man, and cybernetics*, 9, 62-66.
- PEDROTTI, M., WONG, C., EL MOUNTASSIR, G. & LUNN, R. 2017. An analytical model for the control of silica grout penetration in natural groundwater systems. *Tunnelling and Underground Space Technology*, 70, Pages 105-113.
- PERSOFF, P., APPS, J., MORIDIS, G. & WHANG, J. M. 1999. Effect of dilution and contaminants on sand grouted with colloidal silica. *Journal of geotechnical and geoenvironmental engineering*, 125, 461-469.
- PERSOFF, P., FINSTERLE, S., MORIDIS, G. J., APPS, J., PRUESS, K. & MULLER, S. J. 1995. Injectable barriers for waste isolation. Lawrence Berkeley Lab., CA (United States).
- PREWITT, J. & MENDELSON, M. L. 1966. The analysis of cell images. *Annals of the New York Academy of Sciences*, 128, 1035-1053.
- RAYHANI, M. H., YANFUL, E. & FAKHER, A. 2007. Desiccation-induced cracking and its effect on the hydraulic conductivity of clayey soils from Iran. *Canadian geotechnical journal*, 44, 276-283.
- SAFARI, E., JALILI GHAZIZADE, M., ABDULI, M. A. & GATMIRI, B. 2014. Variation of crack intensity factor in three compacted clay liners exposed to annual cycle of atmospheric conditions with and without geotextile cover. *Waste Management*, 34, 1408-1415.
- SCHINDELIN, J., ARGANDA-CARRERAS, I., FRISE, E., KAYNIG, V., LONGAIR, M., PIETZSCH, T., PREIBISCH, S., RUEDEN, C., SAALFELD, S. & SCHMID, B. 2012. Fiji: an open-source platform for biological-image analysis. *Nature methods*, 9, 676-682.
- SOUTHEN, J. & ROWE, R. K. 2007. Evaluation of the water retention curve for geosynthetic clay liners. *Geotextiles and Geomembranes*, 25, 2-9.
- TANG, C.-S., CUI, Y.-J., TANG, A.-M. & SHI, B. 2010. Experiment evidence on the temperature dependence of desiccation cracking behavior of clayey soils. *Engineering Geology*, 114, 261-266.
- TARANTINO, A. 2009. A water retention model for deformable soils. *Geotechnique*, 59, 751-762.
- TARANTINO, A. Unsaturated soils: compacted versus reconstituted states. 5th International Conference on Unsaturated Soil, 2010. 113-136.
- TRUEX, M. J., PIERCE, E. M., NIMMONS, M. J. & MATTIGOD, S. V. 2011. Evaluation of in situ grouting as a potential remediation method for the Hanford central plateau deep

- vadose zone. *Prepared for the US Department of Energy under Contract DE-AC05-76RL01830, PNNL, Richland, Washington.*
- VAN GENUCHTEN, M. T. 1980. A closed-form equation for predicting the hydraulic conductivity of unsaturated soils. *Soil science society of America journal*, 44, 892-898.
- WASHBURN, E. W. 1921. Note on a Method of Determining the Distribution of Pore Sizes in a Porous Material. *Proc Natl Acad Sci U S A*, 7, 115-6.
- WONG, C., PEDROTTI, M., EL MOUNTASSIR, G. & LUNN, R. J. 2018. A study on the mechanical interaction between soil and colloidal silica gel for ground improvement. *Engineering Geology*.